FOI
Defence Research Agency
Information Systems
P.O. Box 1165
SE-581 11 Linköping

Phone: +46 13 37 80 00
Fax: +46 13 37 81 00

www.foi.se

Bistatic RCS measurement on different background surfaces

ERIK ZDANSKY, JONAS RAHM AND ANDERS ÖRBOM

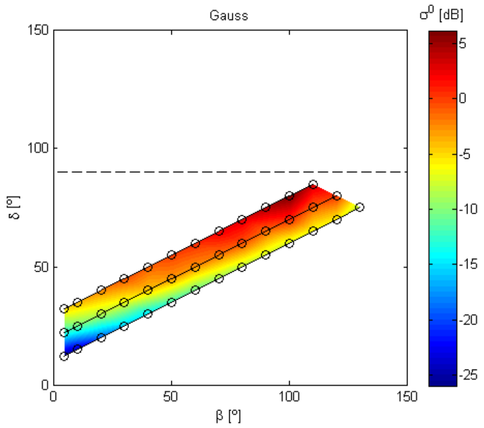

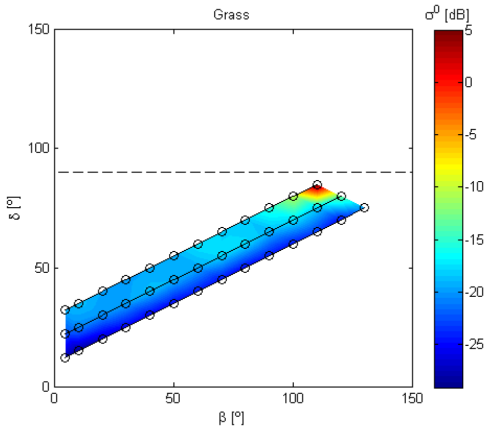

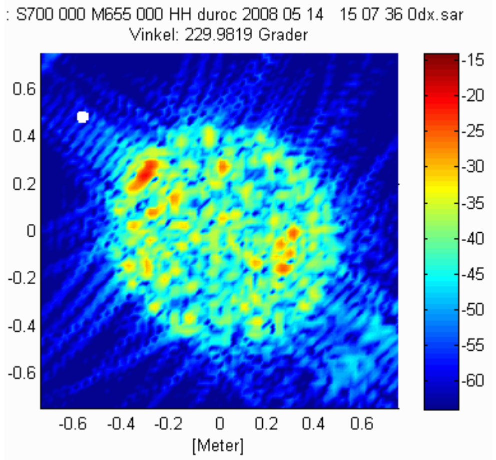

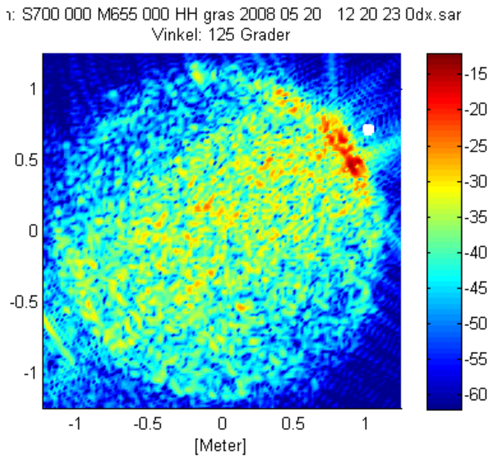

FOI-R--2785--SE Technical report
ISSN 1650-1942 June 2009

Information Systems

Erik Zdansky, Jonas Rahm and Anders Örbom

Bistatic RCS measurement on different background surfaces

Titel	Bistatiska RCS-mätningar på olika typer av markbakgrunder
Title	Bistatic RCS measurements on different background surfaces
Rapportnr/Report no	FOI-R--2785--SE
Rapporttyp Report Type	Teknisk rapport Technical report
Sidor/Pages	37 p
Månad/Month	juni/June
Utgivningsår/Year	2009
ISSN	ISSN 1650-1942
Kund/Customer	FM
Kompetenskloss	Sensor- och signaturteknik
Projektnr/Project no	E3094
Godkänd av/Approved by	Ola Kärvell

FOI, Totalförsvarets Forskningsinstitut
Avdelningen för Informationssystem
Box 1165
581 11 Linköping

FOI, Swedish Defence Research Agency
Information Systems
P.O. Box 1165
SE-581 11 Linköping

Summary

This report accounts for parts of one work package in a Swedish-French cooperation on target and background signatures. The purpose is to report to our partners in this cooperation and to document methods, results and conclusions.

The bistatic reflectivity of a PEC surface with Gaussian height statistics having σ_H=0.0072 m and correlation length L=0.0191 m and of a grass surface have been measured for a series of scattering geometries nominally in the plane of incidence. Three transmitter depression angles, 10°, 20° and 30° have been used together with receiver depression angles from values slightly above the transmitter to 140°, i.e. starting pseudomonostatic conditions and approaching specular geometry at the end of each series. An object-free calibration procedure particularly well suited for bistatic work, which we have previously only tested on calibration objects in pseudomonostatic geometry, has been applied. ISAR imaging and inversion back to RCS data has, together with zero-doppler filtering, been used to check for and remove background contributions. Data has been measured in the frequency range 8 to 12 GHz but due to truncation artefacts only the range 8.5 to 11.5 GHz was used to estimate the reflectivities at 10 GHz. The accuracies of the estimated reflectivities suffer significantly from lacking information on the position of the phase centre, but this could be corrected later once more information is available and a simple method for strongly reducing the vulnerability to this source of error in the future is described. The reflectivity of the Gauss surface increases with transmitter and receiver depression angles, i.e. with the bistatic angle and the bisector depression, although the incoherent part is expected to fall again at high angles. The reflectivities of grass are significantly lower and after some initial increase they form a plateau at -25 to -18 dB depending on the transmitter angle. On approaching the specular geometry the grass signal increases strongly, but this behaviour needs confirmation. The large differences between the two surfaces indicate a need for theoretical models and parameter sets well suited for vegetated surfaces.

Keywords: radar, bistatic, reflectivity, RCS, radar calibration, Gauss surface, grass, X-band, Lilla Gåra

Sammanfattning

Denna rapport redovisar en delinsats i ett svensk-franskt samarbete rörande mål och bakgrundssignaturer. Syftet är att rapportera till våra samarbetspartners och att dokumentera metoder, resultat och slutsatser.

Den bistatiska reflektiviteten för en metalliskt ledande yta med Gaussisk höjdfördelning, σ_H=0,0072 m och en korrelationslängd L=0,0191 m, och för en gräsyta har mätts för en serie av spridningsgeometrier, som alla nominellt ligger i infallsplanet. Tre sändardepressionsvinklar, 10˚, 20˚ och 30˚ har använts tillsammans med mottagarvinklar från strax över dessa värden till 140˚. Detta innebär en kontinuerlig övergång från pseudomonostatiska förhållanden till att mot slutet av serierna närma sig spekulära geometrier. En objektfri kalibreringsmetod, särskilt väl ägnad för bistatiskt arbete, som vi tidigare bara prövat på kalibreringsobjekt i pseudomonostatisk geometri, har använts. ISAR-avbildning och invertering tillbaka till radarmålareadata har, tillsammans med nolldopplerfiltrering, använts för att kontrollera och ta bort bakgrundsbidrag. Data har mätts i området 8 till 12 GHz men p.g.a. trunkationseffekter har bara området 8,5 till 11,5 GHz använts för uppskattning av reflektiviteter vid 10 GHz. De erhållna reflektiviterna lider av en betydande känslighet för saknade uppgifter om magnitudcentrums läge, men detta kan man korrigera för i efterhand om behövliga uppgifter blir tillgängliga och en enkel metod för att framöver starkt sänka känsligheten för denna felkälla beskrivs. Gaussytans reflektivitet ökar med sändar- och mottagardepressionen, d.v.s. med bistatisk vinkel och bisektrisdepression, fast vid högre vinklar förväntas den inkoherenta delen åter falla. Reflektiviteterna för gräs är väsentligt lägre och bildar efter en viss inledande ökning en platå vid -25 till -18 dB beroende på sändarvinkel. Då man närmar sig den spekulära geometrin ökar grässignalen kraftigt, men detta beteende behöver bekräftas. De stora skillnaderna mellan de två ytorna visar ett behov att åtminstone för vegeterade ytor ta fram modeller och parameteruppsättningar som väl beskriver deras bistatiska reflektivitet.

Nyckelord: radar, bistatisk, reflektivitet, RCS, radarmålarea, radarkalibrering, Gaussyta, gräs, X-band, Lilla Gåra

Content

1 Introduction

Sweden (FOI) and France (ONERA and DGA Celar) have jointly decided to address a work programme concerning “New models for radar targets and environment”. The work has been divided into several Work Packages (WPs), see reference [1-2].

The division of tasks between the Swedish and French part is described in reference [1]. The general agreement is that FOI will perform bistatic measurements on different backgrounds and DGA Celar will perform monostatic measurements on targets over different backgrounds. The measurement results will be used for validation and refinements of background models.

The Swedish participation in this work is part of an assignment from the Swedish armed forces to do research within the field of signature modelling.

This report presents bistatic measurements that have been performed at different background samples. This is one of the planned Work Packages (WPs) within the project, see [2]. The measurement campaign was conducted in May 2008 at the FOIs outdoor facility Lilla Gåra. The objective with this WP is to produce a set of bistatic measurement reference data that can be used for validating target-background interaction models in the radar region. The purpose of the report is to communicate the results to our work programme partners and to document measurements procedures and results.

2 Measurement facility

2.1 The test facility “Lilla Gåra”

The RCS measurements, reported here, were conducted at Lilla Gåra [3-4]. Lilla Gåra is the Swedish Defence Research Agency´s outdoor test range for coherent broadband RCS and antenna measurements in the 0.3-110 GHz region see figures 1 and 2.

Figure 1. An overview of the outdoor test facility for RCS and antenna measurements.

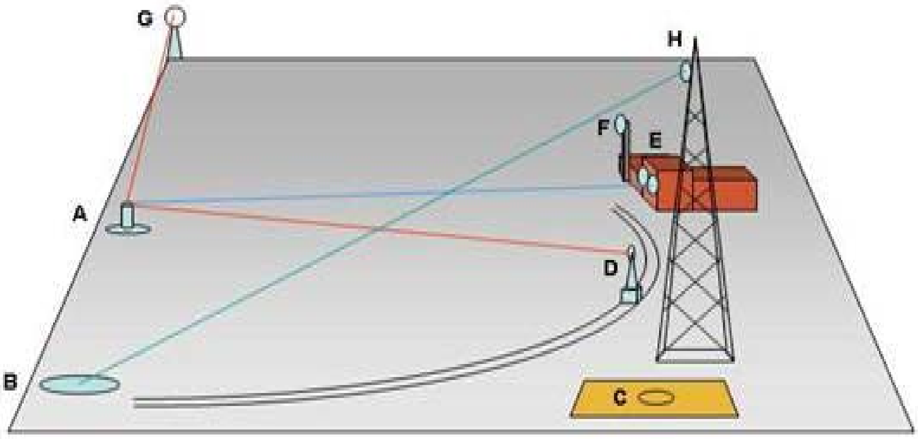

Figure 2. A schematic figure of some examples of different ranges at Lilla Gåra. Free space turntable (A), large turntable (B), marine plane turntable (C), bistatic rail antenna (D), antennas on main building (E), antenna tower on main building (F), east antenna tower (G) and the 50 m antenna tower (H). The colored lines represent some of the possible RCS ranges.

The largest turntable (B in figure 2) has a diameter of 7 m and can manage loads up to 80 tons. It is mainly used for monostatic measurements where the antennas are positioned either in the main building (E in figure 2) at a distance of 162 m or mounted on the 50 m high antenna tower (H in figure 2).

2.2 The bistatic arc

The measurements presented in this report have been performed with the bistatic arc, see figure 3. The arc has been place on a metallic surface and over the turntable at position C in figure 2. The arc consists of a frame structure that supports the arc. The arc has a radius of 3.4 meters and can carry antenna wagons that can be moved independently of each other. The bistatic arc was placed over the centre of a turntable used to rotate the sample while collecting data for bistatic ISAR imaging.

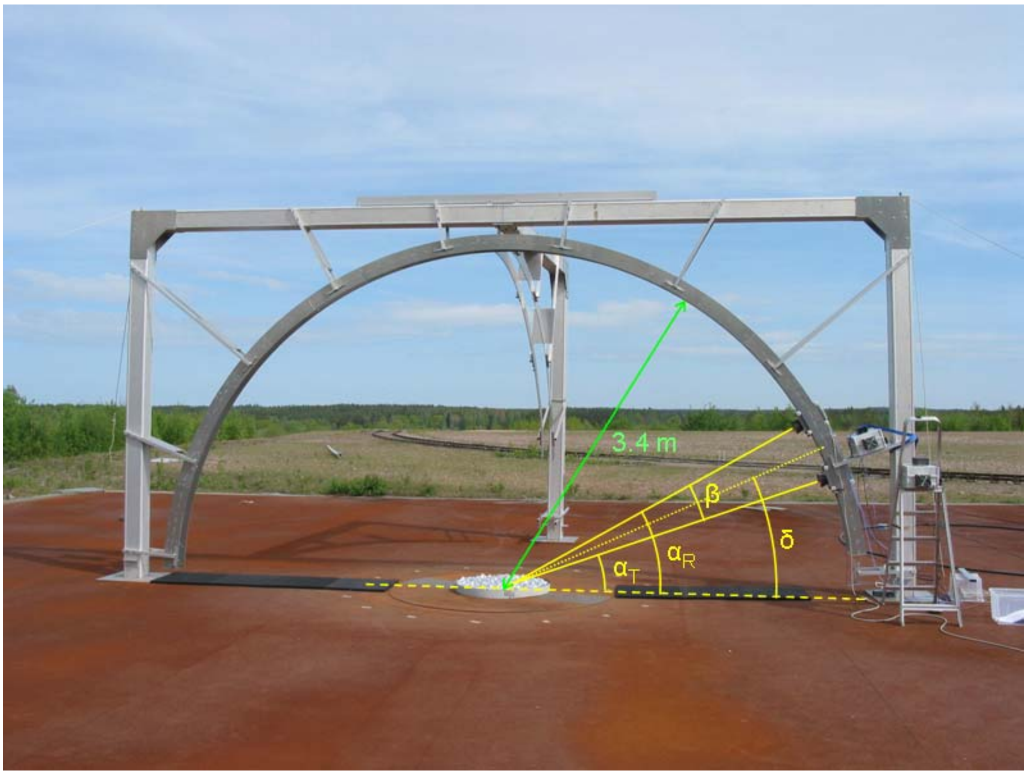

Figure 3. The bistatic arc has an inner radius of 3.4 m and can carry antenna wagons that can be moved independent of each other. Also marked are nominal angles in the plane of incidence, the transmitter and receiver depression angles, α_T and α_R, the bistatic angle, β , and the bisector depression angle δ. Quantities used to describe local scattering geometries are defined mathematically in appendix C.

Figure 4 (left) shows the antennas mounted on the antenna wagons and placed in the arc. The boxes behind the antennas (transmitter and receiver) contain optical links and amplifiers. The temperature in the boxes is stabilized to prevent drift effects in the optical links and amplifiers. The right picture in figure 4 shows a view from the antennas. The black squares are RAM plates and are put there to reduce multiple scattering contributions to the total RCS.

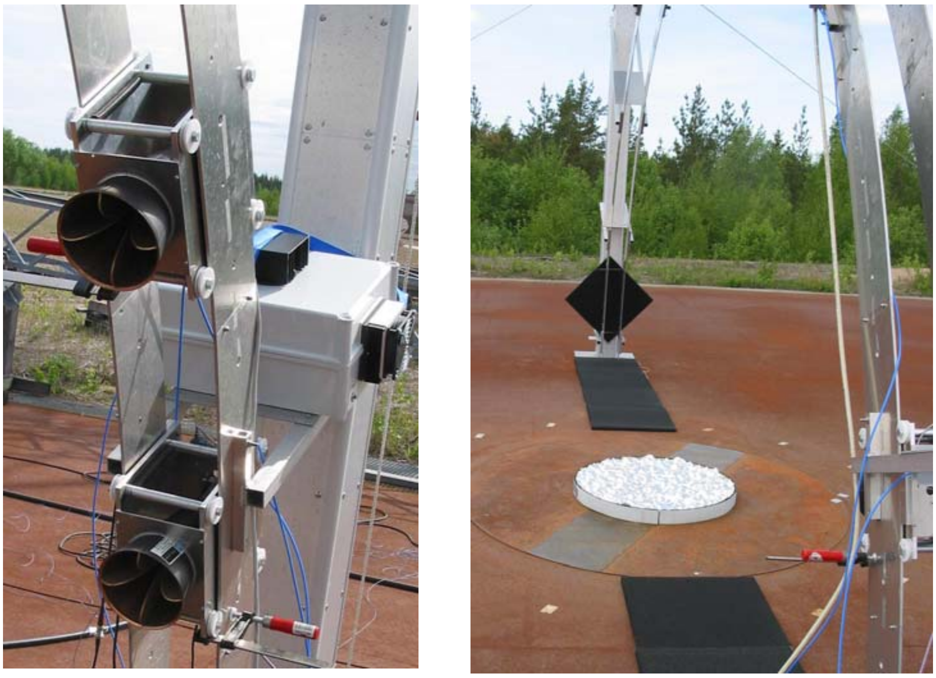

Figure 4-5. The left picture shows the antennas mounted on the arc. The box behind the antennas is the transmitting climate box which contains an optical link and an amplifier. Right picture shows a view from the antenna. The black plates are absorbents (RAM) used to reduce background contributions.

2.3 Equipment

During the measurements the following equipment were used:

- A bistatic arc with an arc radius of 3.4 meters centred above the turntable, see figure 3.
- Ridge horn antennas, Watkins-Johnson P/N 754730-002 A WJ-48461 H, S/N 1048 and 1047, with a gain region of 5 - 18 dB in the frequency range of 2 - 18 GHz. Reference [5] deals with the gain and phase of more or less identical antennas from another supplier (General Instrument D02500).
- Turntable with a diameter of 2.20 m.
- Optical links Miteq MDDT 100M 11G-28-20-M14 and Miteq MDDR 100M 18G-10-20-0 with climate boxes to maintain constant temperature.
- Amplifiers: Transmitter Miteq 6-18 GHz, 30 dB, Receiver Miteq 6-18 GHz, 26 dB.

The external circuit diagram is shown in Appendix A.

2.4 Background surfaces

The different background samples that have been measured are:

- Reference rough metallic surface.
- Flat grass surface

2.4.1 Metallic rough Gaussian surface

The metallic rough surface used for these measurements is made of solid aluminium and has a diameter of 0.9 meter, see figure 4. The surface profile was generated according to the spectrum method used by [6]. In this method a transformation is used to relate a surface correlation function to the power spectral density function in the spatial frequency domain. Using the relation the magnitudes of this density function are found and combined with random phases while making sure that certain symmetries are fulfilled. The spectral density function is then transformed into the height function i.e. the surface. The correlation function used is $C(\tau_x, \tau_y) = \sigma^2 \exp\left[-l(\tau_x^2 + \tau_y^2)\right]$ where τ_x, τ_y are normalised coordinates and l the correlation length normalised in the same way. The roughness of the surface follows a Gaussian distribution function with a correlation length, L, of 0.0191 meters and a height variance, σ_H, of 0.0072meters. This corresponds to kL=4 and $k\sigma_H$=1.5 at 10 GHz. The surface was manufactured from an aluminium block by using a numerically controlled milling machine. Metals, in particular highly conductive metals like aluminium approximate the perfect electric conductor (PEC) used in theoretical work quite well in most cases.

Figure 6. The rough PEC surface. The diameter is 0.9 meter.

2.4.2 Flat grass surface

The grass was placed on a plywood circular disc with a polystyrene border, approximately 70 mm high, see figure 5. The disc, with a diameter of 2.45 meters, was mounted on the turntable. The soil thickness should be large enough to make contributions from the plywood disc and the turntable negligible. In this case this condition was assumed to be fulfilled by using double layer of grass. The two layers, each 20 to 25 mm thick, first layer up-side-down, were placed on the disc. The lengths of the grass leaves were 30 to 40 mm. The humidity was measured by taking a 0.10·0.10 m^2 sample from the upper layer of grass and soil. The moisture content was determined by weighing a sample of the grass before and after drying for ~100 h at 50 ˚C.

Date	Time	Fresh weight [g]	Dry weight [g]	Weight loss [weight %]
080520	15:20	192.3	123.1	36
080521	14:50	235.0	157.5	33
080522	10:05	198.3	137.7	31
080522	14:10	199.8	145.3	27

Figure 7. The circular wooden disc with polystyrene border placed on the turntable. The disc diameter is 2.45 meters. The grass is placed in two layers on the disc.

2.5 Measurement parameters

The parameters that are presented below have been used for all measurements.

Frequencies:	8-12 GHz in 4 MHz steps, i.e. 1001 steps.
Polarisation:	HH (i.e. *E*-field vector parallel to the x-y-plane)
Measurement range:	$r_{\mathrm{transmitter}} = r_{\mathrm{receiver}} = 3.28$ meters measured from the antenna fronts to the centre of the turntable.
Antenna positions:	See table 1 in appendix B and angle definitions in figure 3.
Object rotation angles (ω):	For each antenna position combination the turntable (background sample) will rotate 0-359.95° in 0.05° step, i.e. 7200 positions.
Pulse width:	600 ns
Pulse repetition frequency (PRF):	100 kHz (PRI = 10 μs)

3 Measurement procedure

3.1 Calibration procedure

The object-free calibration data was collected with the antennas pointing to each other between one position on the ground and one on a movable antenna cantilever, see figures 9-10. The directions of the antennas were carefully adjusted using optical methods.

The distance between the antenna faces is 23.07 meters. This antenna distance gives a space loss of around -48 dB (at 8 GHz), sufficient to avoid saturating the system without connecting attenuators to the system. The angle θ, defined in figure 9, is around 22˚, enough to strongly reduce the risk for multipath contributions in the calibration data. Calibration measurements were performed at least once per day.

Shunt data (see 4.1) is available for the May 2008 object measurements but could not be collected with the calibration setup used at that time.

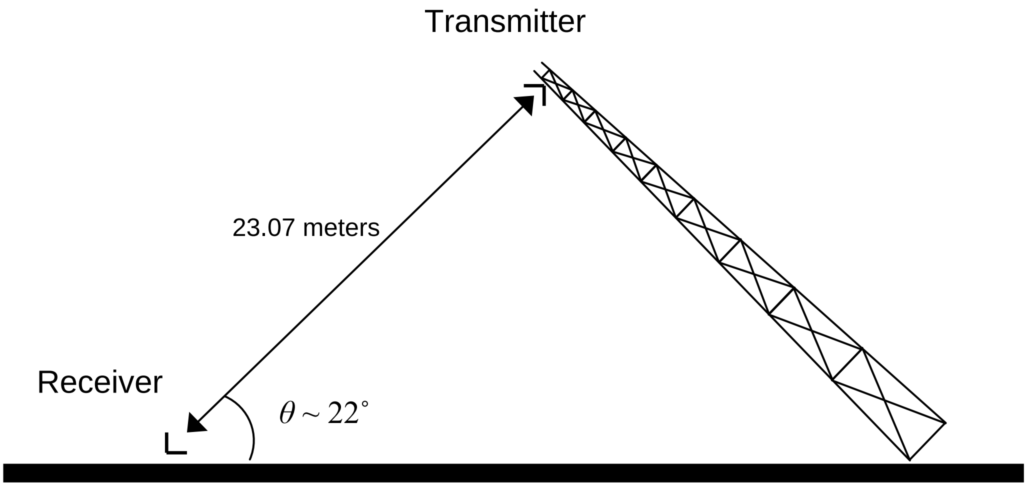

Figure 9. Schematic picture of the object free calibration geometry.

Figure 10. The receiving antenna is mounted on ground and directed to the transmitting antenna on the tilted tower.

3.2 Bistatic measuring procedure

The measurements were collected while rotating the sample surface over 360° on the turntable for each bistatic antenna setting. The antenna angles used are tabulated in appendix B and explained in figure 3. With this procedure we are able to make two-dimensional bistatic ISAR-images for each bistatic geometry. However, the resolution of the images will degrade when:

1. The bistatic angle β increases. This will degrade the monostatic downrange resolution by a factor cos $\beta/2$.
2. The depression angle δ of the radar increases. For a bistatic radar this applies to the depression of the bisector between the transmitter and receiver directions. While this does not degrade the depth resolution *per se*, the projection (perpendicular to the bisector direction) of the resolution length on the ISAR image plane will be longer thus degrading the resolution by a factor cos δ.

The crossrange resolution is proportional to the downrange resolution and will degrade to the same extent. Thus, when the receiver angle is increased, for a constant transmitter angle, this will result in larger bistatic and bisector depression angles and a gradually lower resolution. In addition to this the natural plane of ISAR projection tilts with the bisector direction. The continued use of a horizontal plane means that scatterers found above or below this plane will not project perpendicularly onto the plane which may result in image distortions. For vertical bisector directions this imaging procedure would not produce any resolution at all, other than height, but imaging information could be retrieved by scanning the position of one or both antennas. High bistatic and depression angles will also make the ISAR imaging process more sensitive to errors in geometry parameters.

During the PEC surface measurements two calibration measurements were made before the bistatic measurements started each day and two were made after. During the grass measurements calibration data were only collected before the bistatic measurements began. Shunt measurements (see 4.1) were made between most bistatic measurements. They give some indication of drifts during the day but lacking shunt data for the calibration measurements they cannot be used in calibration as intended.

4 Offline analysis

4.1 Object-free calibration

In these measurement campaigns we have used an object-free calibration method [7-8]. The advantages of this method include that errors in the alignment and in the theoretical RCS estimates of calibration targets are eliminated. The influence from multipath propagation, cross-talk and background can be reduced as well. The method is particularly well suited for calibration of bistatic measurements and has been developed for use in ongoing studies of the bistatic scattering properties of ground surfaces.

According to the radar equation the power received in an object measurement is

$$P_{r,obj} = P_t \frac{G_t}{4\pi R_t^2} \sigma_{obj} \frac{A_r}{4\pi R_r^2} \qquad \Leftrightarrow \qquad \sigma_{obj} = P_{r,obj} (4\pi)^2 R_t^2 R_r^2 \big/ P_t G_t A_r$$

P is power, *G* antenna gain *A* antenna aperture. Index *t* indicates transmitter and *r* receiver.

The purpose of the calibration is to find the unknown, or at least less well known quantities P_t, G_t and A_r, which are assumed to be constant for all measurements. It is sufficient to find an accurate value of their product for each frequency. The power received during calibration with the antennas aligned and pointing at each other at distance R_d is given by:

$$P_{r,cal} = P_t \frac{G_t}{4\pi R_d^2} A_r \qquad \Leftrightarrow \qquad P_t G_t A_r = P_{r,cal} 4\pi R_d^2$$

The object RCS is thus given by

$$\sigma_{obj} = 4\pi \frac{R_t^2 R_r^2}{R_d^2} \frac{P_{r,obj}}{P_{r,cal}}$$

In this expression $P_{r,obj}$ and $P_{r,cal}$ may be replaced by $I_{r,obj}$ and $I_{r,cal}$ (signals proportional to the received power), attenuation (*D*) may be introduced to adjust signal levels and the calibration will depend on frequency.

$$\sigma_{obj}(f) = 4\pi \frac{R_t^2 R_r^2}{R_d^2} \frac{D_{obj}(f)}{D_{cal}(f)} \frac{I_{r,obj}(f)}{I_{r,cal}(f)}$$

In some cases coherent background subtraction may be needed, in particular in the object measurements

$$\sigma_{obj} = 4\pi \frac{R_t^2 R_r^2}{R_d^2} \frac{D_{obj}}{D_{cal}} \frac{\left|\overline{V}_{r,obj} - \overline{V}_{r,obj,bgr}\right|^2}{\left|\overline{V}_{r,cal}\right|^2}$$

In the present measurements "zero-doppler filtering" has been applied, i.e. the contribution from a fixed background has been estimated as the coherent average over all angles.

$\overline{V}$ in the formula above is the complex amplitude signal measured ($I = \left|\overline{V}\right|^2$), but in coherent work one would normally generate calibrated scattering amplitude data, $\overline{S}$ ($\sigma = \left|\overline{S}\right|^2$)[1], rather than scalar RCS-data

$$\overline{S}_{obj} = \sqrt{4\pi \frac{D_{obj}}{D_{cal}}} \frac{R_t R_r}{R_d} \frac{\overline{V}_{r,obj} - \overline{V}_{r,obj,bgr}}{\overline{V}_{r,cal}} \exp\left(\pm \frac{2\pi j}{c_0} (R_t + R_r - R_d) f \right)$$

In this case a phase factor is added to handle differences in phase distance. The sign of the phase is a matter of convention. Additional phase factors may be needed, e.g. to handle the phase of the attenuators.

Instability may cause drift in e.g. transmitter power, P_t. This may be monitored by shunting the transmitter signal, or a constant fraction of it, cP_t, directly to the receiver for reference.

In this case the object RCS is still given by

$$\sigma_{obj} = (4\pi)^2 R_t^2 R_r^2 \frac{1}{P_{t,obj} G_t A_r} P_{r,obj} \quad \text{but} \quad P_{r,cal} 4\pi R_d^2 = P_{t,cal} G_t A_r$$

By using the reference signals $I_{shunt,obj} = cP_{t,obj}$ and $I_{shunt,cal} = cP_{t,cal}$ the RCS may be calibrated despite the drift:

$$\sigma_{obj} = (4\pi)^2 R_t^2 R_r^2 \frac{1}{P_{t,cal} G_t A_r} \frac{cP_{t,cal}}{cP_{t,obj}} P_{r,obj} = 4\pi \frac{R_t^2 R_r^2}{R_d^2} \frac{I_{shunt,cal}}{I_{shunt,obj}} \frac{P_{r,obj}}{P_{r,cal}}$$

In fact, this will also handle other linear drifts e.g. in the receiver gain. If the properties of the antennas are assumed to be constant it should, in principle, be possible to calibrate them once and then use the shunt signal only to follow drifts in the electronic parts of the system for calibration purposes. One drawback of introducing the ratio between two additional quantities into the calibration expression is that it easily adds noise and other disturbances to the calibrated data. In many cases, however, the drift is reasonably frequency-independent, appearing to be a drift in the DC-level of the logarithmic amplitude detector. In such cases the use of a mean correction for all frequencies is probably a reasonable compromise between best drift correction and lowest noise..

4.2 Detector correction, calibration and filtering

The calibration data was inspected with respect to amplitude and phase stability. Each measurement contains 17 different "attenuation steps" (a remnant from an obsolete calibration procedure, now 0 dB is used for all steps) each representing the average over 8 frequency sweeps. Data for the different "attenuation steps" were found to be essentially equal and were averaged coherently. Two calibration runs made directly after each other where also

---

[1] A constant is often included, $\sigma = k\left|\overline{S}\right|^2$, but with the convention used in Columbus $\overline{S}$ is defined so that k=1.

found to be quite similar to each other but in some cases data collected before and after the bistatic measurements had drifted apart far enough that direct coherent averaging resulted in intensities showing a frequency response significantly different from the incoherent average and individual data sets. This was found to be due to phase differences probably caused by small changes in the path length. After reconstruction of the phase (MatLab `unwrap`) linear fits were made. Corrections corresponding to the difference between the linear fit and the average of the fits were then applied to the calibration data sets before forming the averages resulting in coherent averages very close to the incoherent.

A correction handling non-linearities and scale factor errors in the logarithmic magnitude detector was applied to the calibration as well as the object data. On average the correction is modest but for individual values it can be significant and in particular individual calibration values suffering from these non-linearities would affect all the calibrated values for that frequency if not corrected for. The method of finding the correction values is described in [9].

After calibration zero-doppler filtering has been applied to the data in order to remove fixed background contributions. The principle behind this procedure is, as previously described (4.1), that the fixed contributions are estimated as the coherent average over many angles while the expectation value of the average for moving objects on the turntable is zero. Thus, by subtracting the average contributions the difference should represent moving objects. In this work the average over a complete rotation is used but in other cases the average may be formed over some sector less than 360°. Provided that the PEC plate is accurately centred this also reduces contributions from the dihedral its edge forms with the turntable significantly. There are, however, several peaks in the background behind the target area that are only marginally affected. These are likely due to multipath propagation involving the rotating plate. The effect of zero-doppler filtering may thus be used in identifying the multipath involved in forming such peaks. Zero-doppler filtering would also remove fixed specular contributions from the target if present, in particular in areas near its centre. The results can thus be said to represent the incoherent scattering from the rough surface. In terms of scattering amplitudes this may be written $\left\langle \left|\bar{S} - \langle \bar{S} \rangle\right|^2 \right\rangle$. Replacing $\bar{S}$ with $\bar{E}$ and rewriting the expression confirms that this corresponds to the incoherent part which in the theoretical literature on bistatic scattering is usually written as $\left\langle \left|\bar{E}\right|^2 \right\rangle - \left|\langle \bar{E} \rangle\right|^2$. In experimental work drift and noise etc. do not permit the coherent part to be fully removed, but it is usually possible to achieve 10-25 dB suppression for fixed scatterers.

The application of time-domain filters to calibration and bistatic data before calibration has been considered. However, this easily introduces truncation artefacts etc. which can be difficult to handle, in particular for uncalibrated data. The contributions from the background and the bistatic arc including multipath propagation fall outside the area of the PEC target in the ISAR image. Some background contributions may fall inside the images of the grass sample, which is larger, but well outside the central area over which σ^0 is evaluated in this work.

4.3 ISAR imaging

The ISAR-films (sets of images for many angles) were generated using a batch processing bistatic version of the program Columbus. Instead of showing the object rotating on the turntable this program calculates ISAR films so that the radar appears to rotate around a fixed object. Columbus compensates for distance variations across the target[2] but the footprints of the antennas are treated separately. The width of the ISAR sector was selected to give a cross-range resolution matching the downrange resolution resulting from the bandwidth. No filtering (e.g. Hanning) was applied in the imaging procedure. The pixel width of the ISAR images was set to be less than half the resolution (oversampling by a factor of two) as calculated for the given bandwidth and a monostatic horisontal radar geometry. For other geometries the oversampling will be higher since the resolution is lower. One image frame per degree was generated.

The ISAR-images are calculated assuming that scattering takes place at positions in a horisontal plane, the height of which can be adjusted (`z_ground`). This is the natural projection plane for a horisontal radar, but for other geometries contributions from other points will not be mapped in a vertically projected position on this plane.

The ISAR image will be dependent on a correct representation of the measurement geometry and other phase distances. Errors in these parameters typically result in angular-dependent offset positions in the images so that the object appears to "wobble" i.e. there is no fixed centre-point in the image but this point moves in a circle around its expected position, when the ISAR film is viewed. In more severe cases the image will also be defocussed. Geometries with large bistatic angles or steeply inclined bisector directions will be more sensitive to phase distance errors. The prime parameters used to adjust for phase distance are antenna distances (including calibration distance), `z_ground` and a parameter called `range_offset` used to force phase distance changes. In this work measured geometry parameters were found to yield accurate images with only minor wobbling without the use of further adjustments. This wobbling can be reduced by adjustments of the `range_offset` or the `z_ground` parameters. The well defined outer edge of the PEC-plate appears to permit adjustments in the `range_offset` parameter to an accuracy of a few mm or less. The `range_offset` is then found to vary with the geometry, possibly due to small deviations in the antenna arc geometry. However, the manual adjustment of this is very time-consuming and the procedure is therefore not generally applied.

---

[2] For a horisontal monostatic radar the normalisation is such that the RCS calculated from the ISAR image is position independent. However, tests using simulated pointscatter data have unexpectedly shown a significant dependence on radial position and turntable angle for other geometries. This was discovered too late in the work to allow an analysis of the causes. The fact that the ISAR sample images represent many independent scatterers distributed symmetrically around the centre of rotation should also be expected to reduce, but not necessarily remove, the effects of this position-dependence. Fortunately the effect on the average for a single point scatterer over all angles is quite small and the value is normally close to that of a central point scatterer and to the value expected, except perhaps for high receiver α_R-values where moderate deviations have been observed.

Examples of ISAR images are shown in figures 11-16. For pseudomonostatic geometries the dihedral (bruderhedral) formed between the edge of the PEC plate and the turntable gives a strong contribution. Background contributions do show up in the images but are in general modest in strength and reasonably well separated from the area of interest, at least in the PEC plate case. In the grass case the contributions sometimes fall within the sample area but outside the central part presently used for data collection. The more strongly bistatic geometries, which also suffer from high bisector depressions, are seen to suffer from lower resolution and to deformations resulting from intrinsic limitations for these geometries and to the high sensitivity to geometry errors described above. Furthermore, there appears to be a mismatch in crossrange and downrange resolution that varies across the sample area. In the case of the large samples and e.g. strongly bistatic geometries some intensity may spill over out into areas outside the sample due to range ambiguities. Even if this would occur for some of the grass measurements it is not expected to affect the central parts of the images.

4.4 Image editing and extraction of normalized RCS

In order to remove contributions from fixed scatterers, multipath propagation, edges etc. the ISAR films are cropped so that only the central part of the images remain with pixels outside set to zero. For the PEC plate the central part was chosen as a circle 0.7 m in diameter. This is, of course, a compromise. A smaller area would give an additional margin to the edges and the local scattering geometry will deviate less from the nominal geometry. However, more of the signal will be lost, the statistical basis will be smaller and truncation effects will be stronger. Antenna tapering will modify the effects of film cropping. For the grass the same crop size was used to make the results more comparable. Pixels falling on the rim of the central area will be retained if its centre falls within the cropping radius, i.e. pixels are either inside or outside, not fractional. In principle different parts of the same image frame may be used to provide data for different scattering geometries.

This procedure can be expected to introduce some truncation artefacts when the films are inverted back to the frequency-angle domain. The artefacts are mainly found at the edges of the frequency range, which are sacrificed.

After the film frames have been cropped the effective area is calculated. Since distance compensation was included already in the generation of the ISAR films [4.2 footnote 2] only the directivity of the antennas need to be taken into account. The transmit and receive antennas are of the same type and the antenna pattern has been measured. The direction from the antenna to each pixel is calculated and then transformed to the angles in the antenna system used during antenna measurement. The relative antenna sensitivity for each pixel is then found by interpolation in the experimental data. An array of such pixel sensitivities corresponds to the footprint of one antenna and the product of transmit and receive footprints forms the radar footprint[3]. The footprints are

---

[3] Remember that the ranges to individual pixels is not included in the footprints considered here. Furthermore the footprint should be calculated as the average over all directions in the sector used to generate the ISAR

cropped like the ISAR frames and the effective area is the sum of pixel values multiplied by the pixel area (or more accurately the integral of the antenna sensitivity product across the footprint). The sample area used is well illuminated so the effective area does not differ very much from the geometric area.

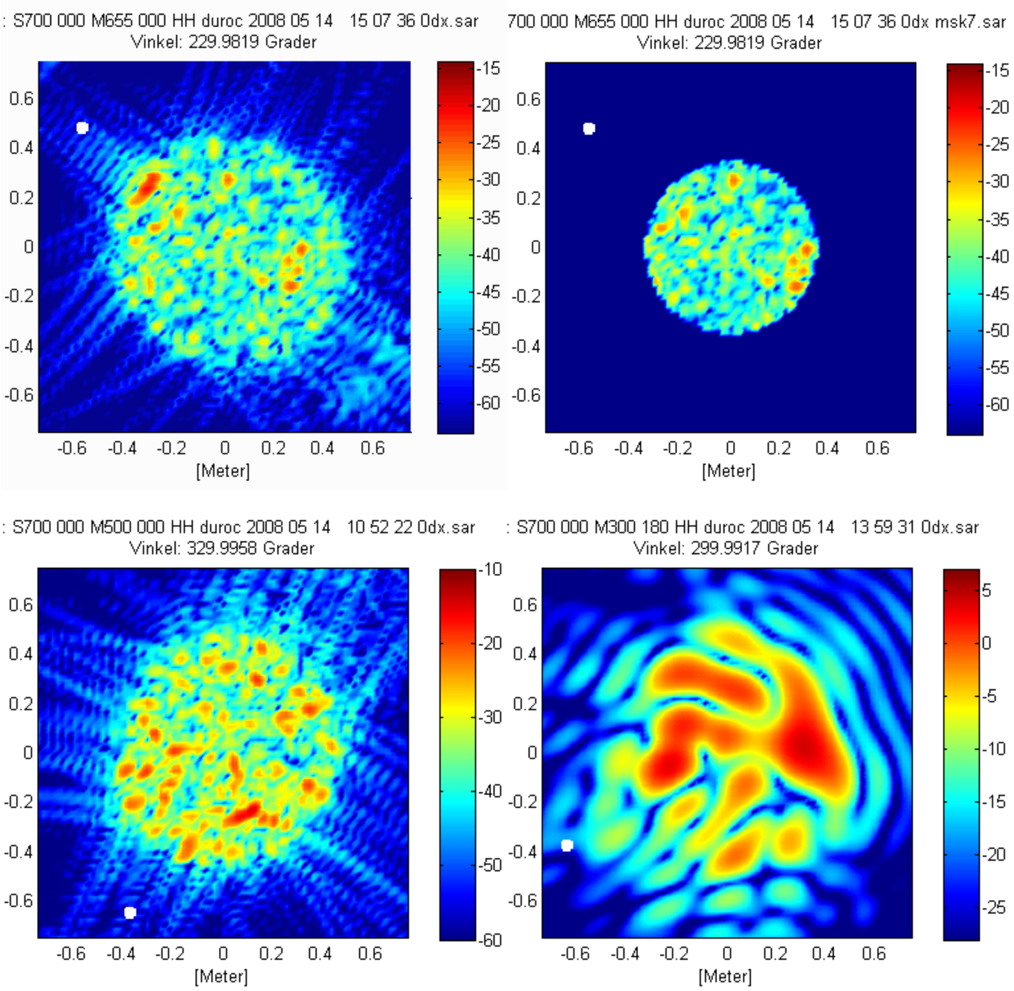

Figures 11-14. Sample frames from the ISAR-films of the Gauss surface measured in different geometries. Top left $\alpha_T = 20^\circ$, $\alpha_R = 24.5^\circ$, *with remnants of the front dihedral and weak background contributions* ($x = 0.6$, $y = -0.5$) *visible despite zero-doppler filtering. The white dot marks the direction to the radar. Top right the central part of this film frame used for extraction of* σ^0. *Bottom left, at* $\alpha_T = 20^\circ$, $\alpha_R = 40^\circ$, *the front dihedral is no longer significant. Bottom right, at* $\alpha_T = 20^\circ$, $\alpha_R = 120^\circ$, *the increase in the bistatic angle and the bisector depression has already reduced the resolution strongly.*

---

frame. However, the intensity integral over a circle at the centre of the footprint should be the same for an individual direction as for the average over all sector directions.

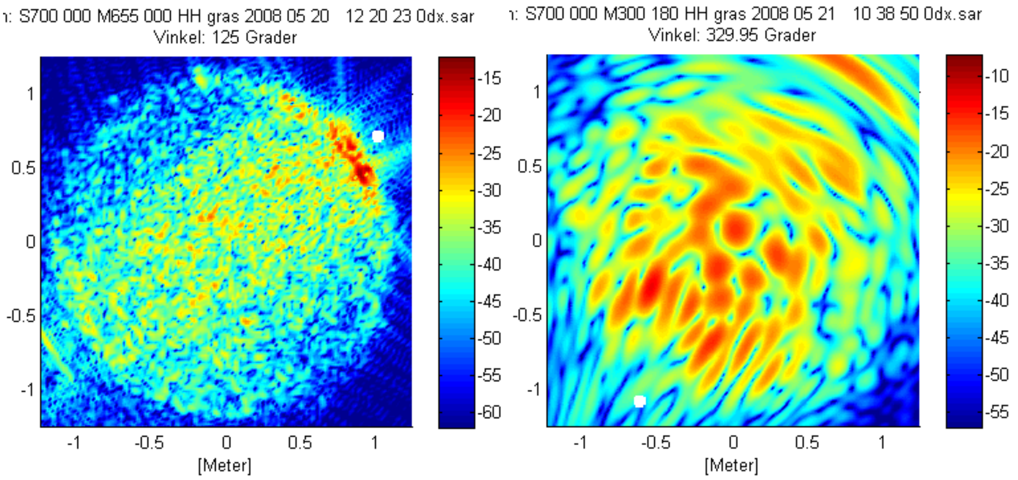

Figures 15-16. Sample frames from the ISAR-films of the grass surface measured in different geometries. Top left $\alpha_T = 20^\circ$, $\alpha_R = 24.5^\circ$, *with the front dihedral and weak background contributions (x = -1.1, y = -0.65) visible despite zero-doppler filtering. Right* $\alpha_T = 20^\circ$, $\alpha_R = 120^\circ$, *not only has the increase in the bistatic angle and the bisector depression reduced the resolution, but there is a pronounced mismatch between downrange and crossrange resolution which varies across the surface.*

The antenna sensitivity is here treated as a scalar, i.e. the phase is not taken into account. This should be a valid approximation, atleast as long as the angular dependence of the antenna phase centres can be neglected, cf. app. E. At sample positions too far of the boresight direction of one or both antennas it is not unlikely that careful corrections for phasefront errors are required for structured targets and that it could be difficult to achieve good results despite such precautions. It is thus probably wise to avoid relying on data collected far out from the antenna boresight directions. The situation may, however, be different for clutter samples[4]. Here, even if minor parts of the area used in these experiments would be affected by this kind of phase related errors their weight in the footprint-corrected averages are expected to be low.

The measurements have been made for HH-polarisation, i.e. they are not full-polarimetric. In addition to the true HH- scattering contribution cross polarisation sensitivity of the antennas could add contributions to the signal. These could involve crosspolarisation in both antennas and VV-scattering in the sample or one antenna and crosspolarisation scattering in the sample. Similar contributions may be present in the antenna data too, but one should

---

[4] More exactly, to get the correct magnitude for an off-boresight ISAR pixel it is required that the relative phases of the underlying scattering amplitude data are correct. In the frequency direction this will be taken care of if phase calibration is included (or not needed). However, in the angular direction corrections could be needed if the phase centre moves significantly for the geometry variation caused by moving the pixel over the turntable angle sector used for generating the image. More relevant for the σ^0 results is the ISAR-inversion. It is assumed that this process recreates all input contributions. I.e . if no corrections are applied the contribution from the off-boresight position will have phase error determined by the antennas and would normally be weaker than that from a central pixel. Since we are interested in the clutter level i.e. the sum of many incoherent contributions from independent scatterers phase errors might be expected to have little influence on the average and the weaker magnitude could still be handled by the footprint correction. In the case of a structured target it is required that the relative phase of all contributing pixels are the same in order to get inverted data of the correct magnitude.

not expect them to simply cancel. According to [5] the cross-polarisation sensitivity for these antennas is estimated to be at least 25 dB below the copolarisation sensitivity. The effects are thus expected to be small and are not included in the footprint estimates. To include a correction for them would require at least an elaborate polarimetric calibration of the antennas.

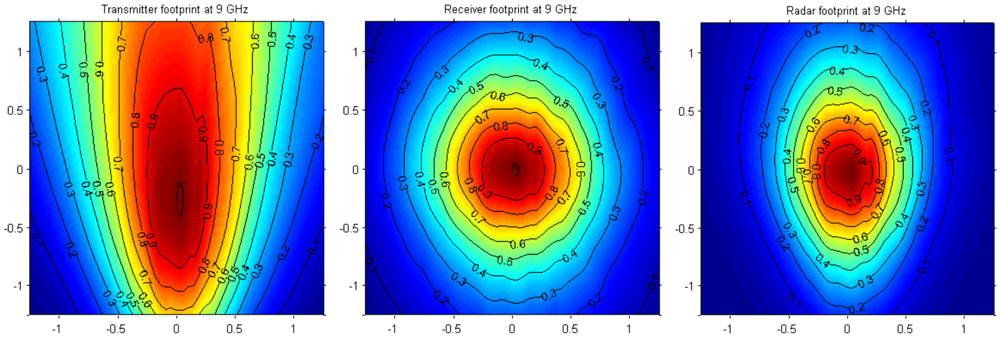

Figures 17-19. Examples of calculated footprints for the transmitter, the receiver and their product, i.e. the radar footprint at 9 GHz for $\alpha_T=20^\circ$*,* $\alpha_R=90^\circ$*. Contours mark the relative intensity in linear units. These footprints only reflect antenna directivity, not the local antenna range. The radar footprint is cropped liked the ISAR frames and then integrated to give the effective area.*

The cropped films are inverted back to the frequency-angle space and normalised using the effective areas. Inverted values have been calculated for 0.04 GHz steps in frequency and 1° steps in angle. The result is then incoherently averaged over all angles. Figures 20-21 show examples of this. The outer parts of the frequency range are, as mentioned, affected by truncation artefacts and therefore discarded. A linear fit (of intensities in dB) is then made for the 8.5 to 11.5 GHz frequency range and the fit value for 10 GHz is used as an estimate of σ^0 at 10 GHz at that geometry. The fit also yields values for $d\sigma^0/df$. These values are only reported in appendix D due to excessive data scatter.

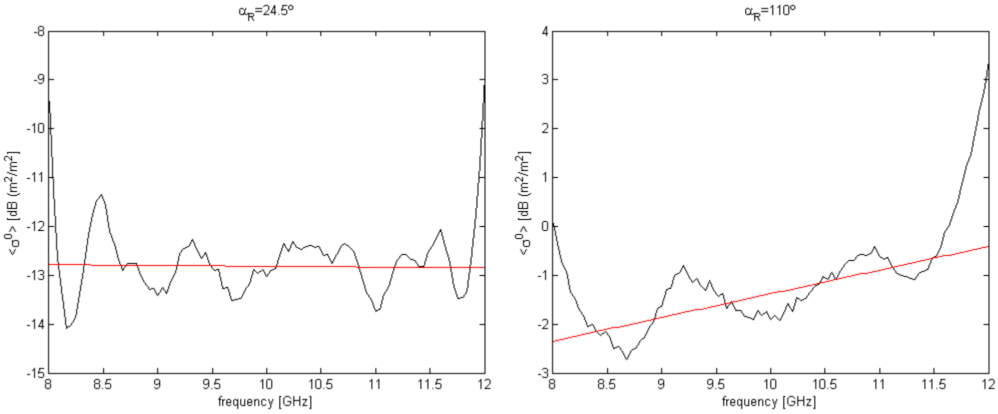

Figures 20-21. Examples of the reflectivity as a function of frequency and mean over all turntable directions (film frames). Gauss surface, $\alpha_T = 20^\circ$*.*

4.5 A short notice on error sources

According to [8] antenna alignment can be expected to be one of the more important sources of errors in this type of calibration procedure. Multipath propagation and interference could also lead to significant errors but here emphasis has been put on avoiding this. Unfortunately the lack of calibration shunt signals does not permit a compensation for radar sensitivity drift as described in section 4.1.

The short distance used, together with the $1/R^2$ dependence for one and $1/R^4$ dependence for two antennas make the calibration vulnerable to errors in this distance. It must be stressed that the good images and small wobbling found for the distances used only indicate that the difference in distances between the calibration and measurement geometries has been accurately measured. These distances refer to the fronts of the antennas and this position is not necessarily the "magnitude centre". Appendix E demonstrates that in this case one may need to add up to 1.4 dB to the results reported but also proposes methods for strongly reducing this error. A few other antenna-related error sources have previously been briefly discussed in section 4.4.

Note added in proof: Measurements and checks made after the addition of appendix E indicate that 0.06 dB should be subtracted from the values given in this report to correct for the position of the "magnitude centre". Other sources of error are then likely to be dominant.

5 Results

5.1 Reflectivity

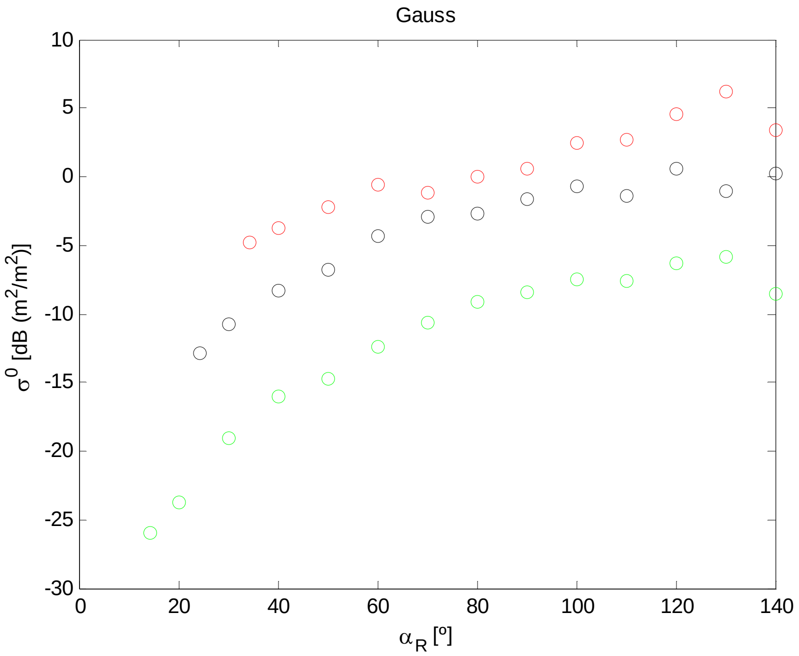

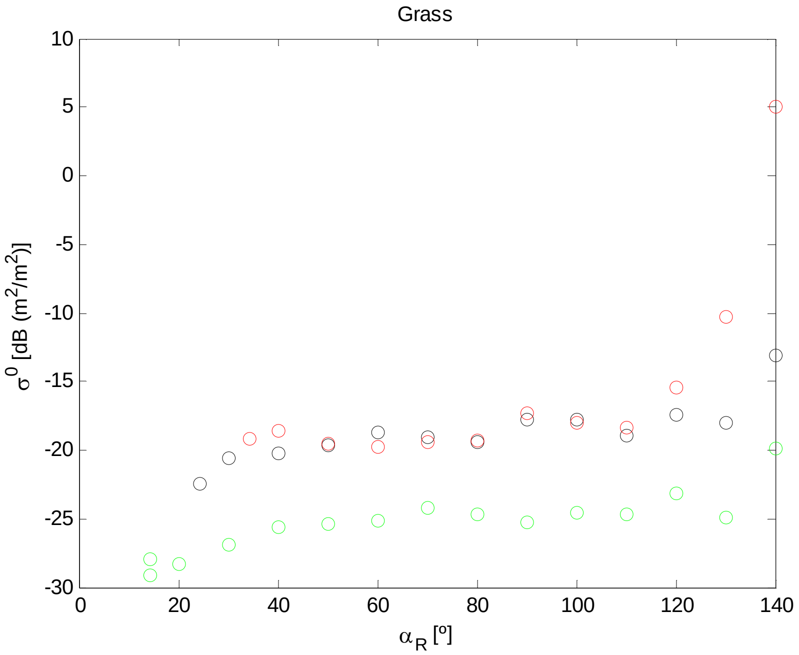

Figures 22-23. Extracted σ^0 *values for the Gauss and grass sample surfaces at 10 GHz and HH polarisation as a function of the nominal receiver angle* α_R*. Green circles nominal transmitter angle* α_T*=10˚, black 20˚, red 30˚.*

The normalised results are displayed in figures 22-27 and tabulated in appendix B. Figures 24-27 display the range of angles nominally covered by our measurements and the strength of the reflectivity at these angles.

The reason for presenting the reflectivity results in figures 24-27 also is to emphasize the multidimensional character of the data. The geometry is described using either the same angles α_T and α_R or an alternative set of basis angles, the bistatic angle β and the bisector depression δ. It is our hope that these diagrams will better visualise how the reflectivity varies with the scattering geometry. They are also better suited to display how a geometry relates to special cases like monostatic and specular conditions[5], symmetries, and to illustrate the fraction of geometries covered etc.

It should be kept in mind that all these geometries are nominally restricted to the plane of incidence and thus represent only a minor, although important, fraction of all geometries. This fraction can for an isotropic surface be described as a two-dimensional swath through a three-dimensional space. An anisotropic surface would need four dimensions to describe the scattering geometry, and a complete polarimetric description would also require more dimensions. Appendix C discusses how the local geometry deviates from the nominal. The extracted information on frequency dependence and a brief discussion on this is found in appendix D.

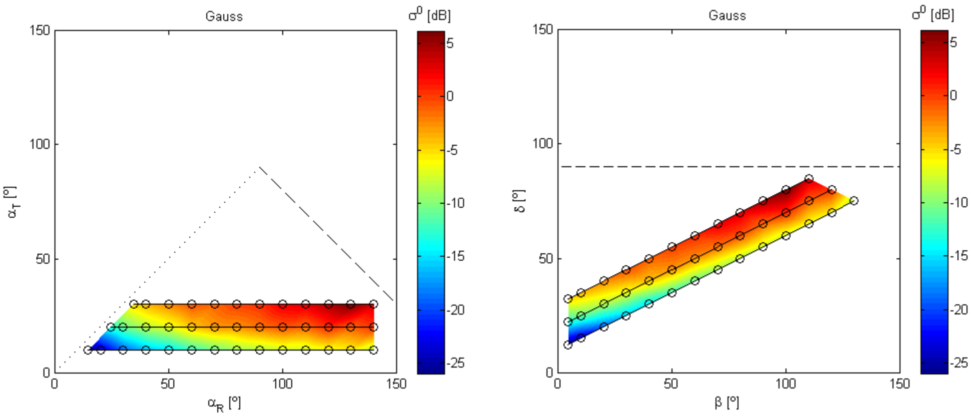

Figures 24-25. The geometry range covered by the measurements made for the Gauss sample surface. In the left diagram the geometry is expressed in α_T and α_R while in the right they have been converted into the bistatic angle β and the bisector depression δ. The dotted line represents monostatic conditions. Due to reciprocity α_T and α_R may be interchanged, so the data may be mirrored in this line. In the right diagram monostatic conditions plot along β=0, of course. The dashed lines represent specular condition. All geometries nominally involve directions in the plane of incidence only.

---

[5] Here the geometry is considered to be specular if a smooth sample surface would reflect the incident beam in the direction to the receiver, but if the surface is rough there will not be specular conditions. The Rayleigh specularity criterion draws the line between rough and smooth at $\sigma_H = \lambda/4\pi \sin\alpha$ giving a mean square value for the "specularity coefficent" $\langle\rho_S^2\rangle=0.085$. At 10 GHz and α=10, 20 and 30° the limiting value for σ_H is 22, 11 and 7.5 mm, respectively.

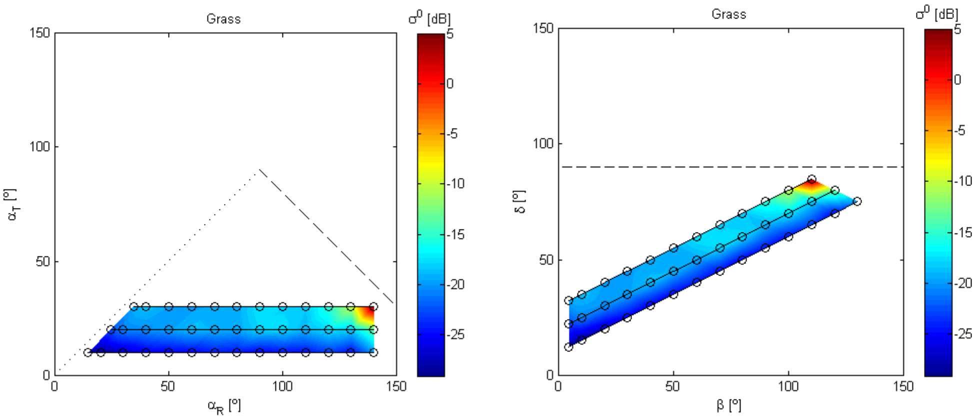

Figures 26-27. The corresponding data for the grass surface. Please note different colour scale limits.

5.2 Discussion

The reflectivity curves for the Gauss surface are generally in good agreement with calculated curves [10]. This, of course, adds to the confidence we have in our data. For low α_R there is initially a fast increase in reflectivity as α_R increases, i.e. on leaving the monostatic geometry. After the initial increase the rate slows down but is still significant, no plateaus form in the curves. Calculated curves [10] show that at higher angles the curves first dip gently before diving steeply as incoherent scattering gives way to coherent at high angles. This range is barely reached in these measurements and it is more difficult to separate incoherent and coherent scattering in experimental work, so the curves only show a hint of this.

The grass reflectivity is in general much lower and the character of the reflectivity curves is different. There is an initial reflectivity increase as α_R increases above the pseudomonostatic value. After this initial increase a plateau is reached. Whether this level is the same for $\alpha_T=20^\circ$ and $\alpha_T=30^\circ$ must be left to future investigations. Finally there is a tendency for the reflectivity values to increase strongly, which is most marked for $\alpha_T=30^\circ$. This increase is most likely coupled to the approaching specular conditions, which the $\alpha_T=30^\circ$ reaches more closely. Whether it is a true increase in the incoherent reflectivity or an increase in coherent reflectivity that has not been cancelled by the zero Doppler filtration must also be left for additional investigations. Non-cancelled crosstalk must also be kept in mind as a plausible cause, but lower α_T values would be expected to give more crosstalk. Due to the higher signal level for the Gauss plate sample a similar signal contribution would not stand out so markedly.

6 Conclusions

The methods used for data collection, calibration and processing have proven successful. The background contributions are usually modest and they are well separated from the sample signal permitting reliable results to be extracted. The object-free calibration method reduces many of the problems associated with calibration objects and in particular the crosstalk which is otherwise a severe problem with these antennas at short range. Shunt calibration needs to be implemented, and this has indeed been done in later measurements not yet reported. As mentioned it has been found that certain radiometric issues in the inversion of ISAR films need to be adressed. In its present implementation the method is limited to surfaces of modest size.

The method has the potential of supplying bistatic reflectivity data for direct application or for comparison with theoretical models over a wide range of scattering geometries although it is not yet established how close to limiting cases, e.g. specular geometries it may provide reliable results. The measurements have so far covered just a few surfaces and all nominal geometries represent scattering within the plane of incidence, i.e. a minor fraction of geometry space.

The data collected so far must be applied in other work or more data amassed for comparison between different situations before much can be said about the results themselves. However, it may already now be concluded that while the Gauss surfaces are well suited for testing the measurement procedure and of significant theoretical interest the major differences between Gauss and grass surfaces clearly indicate a need for surface models (or at least parameters) better suited for modelling ground (at least vegetated ground).

In order to collect the volumes of data needed for future work further developments for the collection and treatment of data are needed. This may include automatic antenna scanning and exploitation of the variation in local geometry across the surface of large samples. Geometries with high bisector depressions may require angular variations in two dimensions to provide the resolution needed to separate the sample signal from background signal.

7 References

[1] Technical Arrangement No. 4.4 ‘New models for radar targets and environment’ FOI Diarie nr. 08-H184:2

[2] Work Breakdown Structure (WBS) of Technical Arrangement No 4.4. Draft date 080615

[3] S. Nilsson, M. Wilow, N. Karlsson och A. Örbom, "Improvements of the Swedish outdoor RCS measurement capability", *AMTA Europe Symposium*, München, 1-4 maj 2006, Conference proceedings 118-123.

[4] J.Rasmusson, N. Gustafsson och J. Rahm, "Outdoor broadband RCS measurements of model-scale aircraft", *AMTA*, Cleveland USA, 3-8 november 2002 Conference proceedings 439-444 (FOI-S--0698-SE).

[5] L. Pettersson, "Determination of gain and phase for a standard gain antenna", FOI-R—2046—SE Linköping 2006.

[6] "Experimental studies of bistatic scattering from two-dimensional conducting random rough surfaces" by T.-K. Chan, Y. Kuga, A. Ishimaru and C.T.C. Le, IEEE Trans. on Geoscience and Remote Sensing 34(3) (1996).

[7] E. Zdansky, "Kalibrering av radarmålarea, särskilt objektfri kalibrering", FOI-R--2442-SE Linköping 2007.

[8] E. Zdansky, A. Örbom, "Kalibrering av logaritmisk magnituddetektor", FOI-R--2441-SE Linköping 2007.

[9] E. Zdansky, A. Örbom, "Prov med objektfri kalibrering av radarmålarea", FOI-R--2443-SE Linköping 2007.

[10] M. Gustavsson *et al.* to be published

[11] C.A. Balanis, Ch. 12.7 in "Antenna theory", John Wiley & Sons 1982, ISBN 0-471-60352-X

Appendix A: Block circuit diagram

Block circuit diagram of external parts of the measurement radar.

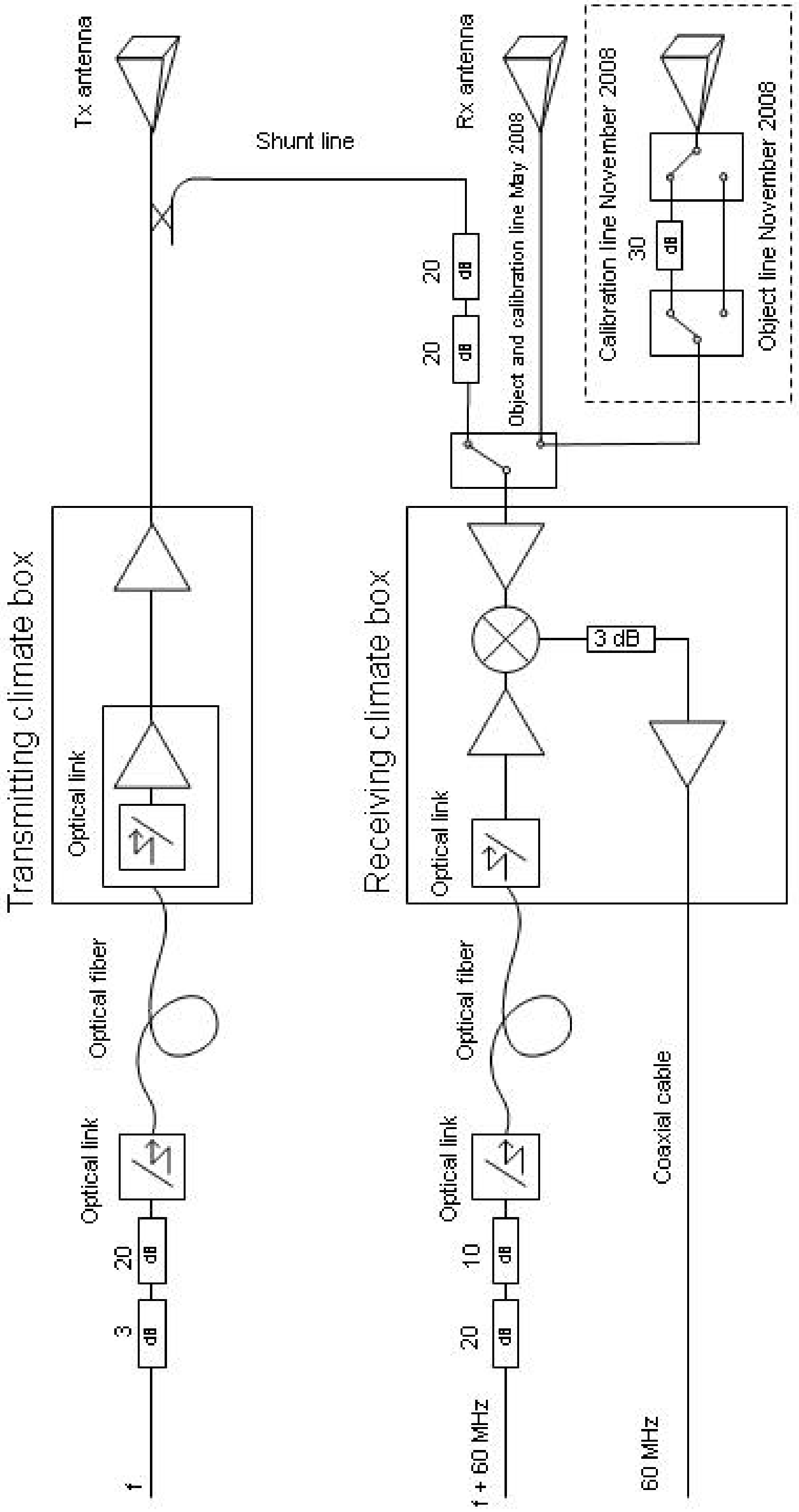

Appendix B: Measured reflectivity

The table below presents results for the different antenna angle combinations for the grass and metallic Gauss surfaces. The polarisation is HH and the antenna depression angles, *α*, of the transmitter, T, and receiver, R, are defined in figure 3. Please refer to 4.5 and appendix E for error discussions and in-proof correction (add 0.25 dB to these values).

Angle combination	α_T	α_R	σ^0_{Gauss} [dB] (10 GHz)	σ^0_{grass} [dB] (10 GHz)
1	10°	14.5°	-26.0	-29.1
2	10°	20°	-23.8	-27.9
3	10°	30°	-19.1	-28.4
4	10°	40°	-16.1	-26.9
5	10°	50°	-14.7	-25.6
6	10°	60°	-12.3	-25.3
7	10°	70°	-10.6	-25.1
8	10°	80°	-9.1	-24.3
9	10°	90°	-8.5	-25.3
10	10°	100°	-7.5	-24.5
11	10°	110°	-7.6	-24.7
12	10°	120°	-6.4	-23.2
13	10°	130°	-5.8	-24.9
14	10°	140°	-8.5	-19.9
15	20°	24.5°	-12.8	-22.5
16	20°	30°	-10.7	-20.6
17	20°	40°	-8.3	-20.2
18	20°	50°	-6.7	-19.6
19	20°	60°	-4.3	-18.7
20	20°	70°	-2.9	-19.0
21	20°	80°	-2.7	-19.4
22	20°	90°	-1.7	-17.8
23	20°	100°	-0.7	-17.8
24	20°	110°	-1.4	-18.9
25	20°	120°	0.6	-17.4
26	20°	130°	-1.1	-18.1
27	20°	140°	0.2	-13.1
28	30°	34.5°	-4.8	-19.2
29	30°	40°	-3.7	-18.5
30	30°	50°	-2.3	-19.5
31	30°	60°	-0.6	-19.8
32	30°	70°	-1.2	-19.4
33	30°	80°	0.0	-19.3
34	30°	90°	0.6	-17.3
35	30°	100°	2.5	-18.0
36	30°	110°	2.7	-18.3
37	30°	120°	4.6	-15.4
38	30°	130°	6.2	-10.3
39	30°	140°	3.3	5.0

Appendix C: Local vs. nominal scattering geometry

As pointed out in section 5.1 it should be remembered that the local scattering geometry varies across the sample surface. Figure C1 illustrates this for a nominal transmitter depression angle of 20°. For symmetry reasons only one half of the 0.7 m diameter sample surface needs to be considered. The black lines correspond to local geometries along the diameter where the plane of incidence intersects the sample surface, here taken to be 0.05 m above the turntable surface. The red curves correspond in the same way to the circular part of the perimeter. In order to avoid ambiguities and values folding back the local scattering geometry is expressed in selected directional cosines of the directions of incidence and scattering. The local coordinate system and angles are defined at the end of this appendix.

For the direction of incidence only the cosine of the local angle of depression α_T is needed (provided that the surface is isotropic). Low values of cos α_{scat} imply backscatter (e.g. pseudomonostatic) geometries while higher values imply larger bistatic angles. It can be seen that for the pseudomonostatic values the variation in local geometry is essentially the same on the perimeter as along the intersection with the nominal plane of incidence, and that cos φ_{scat} values are low, i.e. the contribution from out of plane scattering is small. For the more bistatic cases the range of α_R and α_{scat} variation is still determined by points along the diameter but the local out-of-plane scattering geometries can be seen to gain in importance (cos φ_{scat} increases).

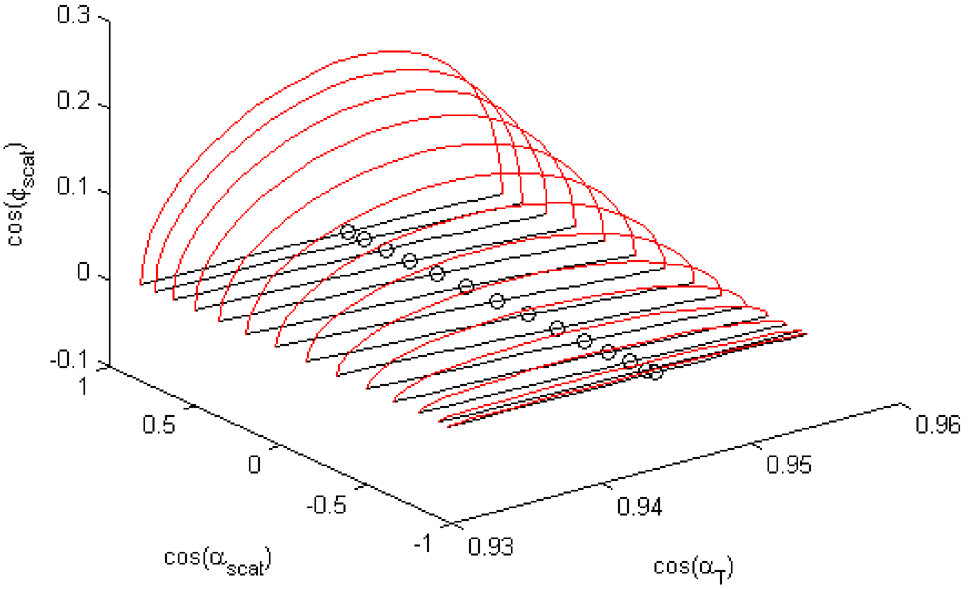

Figure C1. Variation in local scattering geometry for various nominal scattering geometries α_T=20° α_R=24.5 to 150° (the limit in the measurements was 140°). The nominal geometry is given at the centre of the turntable, i.e. slightly below the sample surface. Circles represent the geometry at the centre of a 0.05 m thick sample surface, the black lines geometries along the sample's intersection with the plane of incidence and the red curves represent one half of the sample perimeters. See text for details on the directional cosines used to represent the local geometry.

The local geometry coordinate system [u, v, w] and angles are defined by the plane of incidence and the sample plane as follows. Let $\hat{i}$ be the direction of incidence, pointing from the transmitter to the point [x, y, z_{gnd}] on the surface for which the local geometry should be calculated. Let $\hat{s}$ be the scattering direction from that point to the receiver. The local system can now be defined by:

$$\hat{u} = \frac{\hat{i} \times \hat{s}}{\left|\hat{i} \times \hat{s}\right|}$$

$$\hat{v} = \hat{w} \times \hat{u}$$

$$\hat{w} = \hat{z}$$

The directional cosines needed are components defined by scalar products:

$$\cos\alpha_T = \hat{i} \cdot \hat{u}$$

$$\cos\alpha_{scat} = \hat{s} \cdot \hat{u}$$

$$\cos\varphi_{scat} = \hat{s} \cdot \hat{v}$$

Please note that these angles are measured between the scattering direction and the two horizontal principal axes respectively of the local coordinate system. The α_{scat} and φ_{scat} are thus not measured in principle planes of the local system, unless the scattering direction belongs to such a plane, i.e. if the scattering source lies along the diameter where the sample intersects the plane of incidence.

Appendix D: Frequency dependence

Figures D1-2 show compilations of the mean frequency dependence in the range 8.5 to 11.5 GHz as obtained from the linear fits.

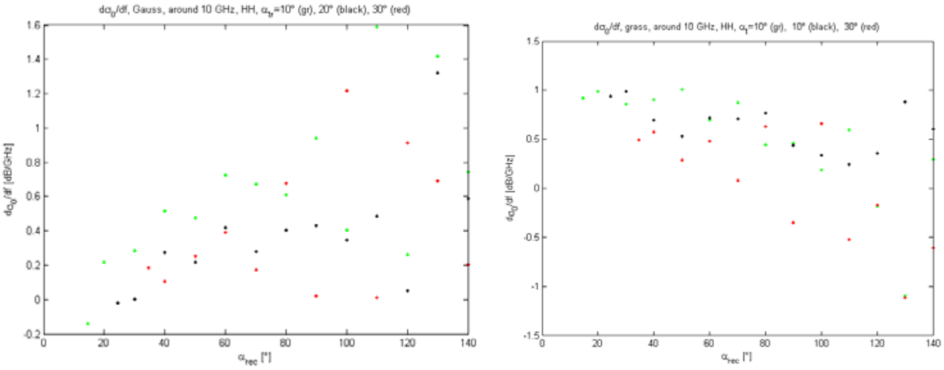

Figures D1-2. Estimated frequency dependence around 10 GHz for the samples and geometries studied. Colours as in figures 22-23.

The spread in data points is partly, in particular for high α_R values, quite large and the results must be treated with caution. The comments given here should thus be viewed as tentative speculations on unconfirmed results.

The large spread for high α_R values may be due to poor statistical support as a consequence of the lower resolution, but the data treatment in this region is also more sensitive to geometrical errors. In most cases there is a tendency for σ^0 to increase with frequency ($d\sigma / df > 0$). For reference it may be interesting to compare with the expected values for spherical surfaces (no increase) and for singly curved surfaces

$$(\sigma \propto f \quad \Leftrightarrow \quad \frac{\partial}{\partial f}\frac{\sigma}{[dB]} = \frac{10}{\ln 10 f} \approx 0.43 \text{ dB/GHz at 10 GHz}).$$

For the Gauss surface the frequency dependence appears to be weaker at lower α_R. Above α_R=90˚ the average may form some kind of plateau, but the data points are very scattered.

For the grass surface the dependence on α_R is reversed. This may be interpreted as due to increasing absorption as α_T and α_R increase. One must also keep in mind that for high α_R (i.e. high β) the rays hitting points at the sides of the sample need to scatter more out of the plane of incidence which they may be expected to do more weakly. For low α_R values the frequency dependence is rather strong and positive in contrast to what might be expected from absorption considerations. One plausible explanation is that the characteristic size, in wavelengths, of the grass leaves and other scatterers fall in the intermediate range where the increase in their scattering power is strong. It must be stressed that the discussion on frequency dependence is very tentative and that the spread in data points limits the ability to draw any firm conclusions.

It could be argued that the scatter in these data indicates that the two parameters used in fitting is one too many, and that the fitting should be replaced by a one-parameter fit, i.e. some type of averaging, in the estimation of σ^0(10 GHz).

Appendix E: Estimation and cancellation of antenna distance offsets

Introduction

In many cases, such as the application of the radar equation it is assumed that at some distance from the antenna, called the far-field region, the radiated power will propagate as spherical waves, at least along the boresight direction. The centre from which these wavefronts propagate is called the phase centre. We will here instead discuss the magnitude centre, the point from which distances should be measured in order to apply the $1/R^2$ intensity range dependence. It is tempting to assume that the phase and magnitude centres coincide, and this is often done such as in the expression, $\frac{e^{-jkR}}{R}$, for a spherical wave. Here we have decided to make a formal distinction between the two concepts.

The concept of a phase centre is sometimes challenged, and it is an approximation. Like the radar equation, the far-field, and spherical wavefronts it is a useful approximation and, if not valid, these approximations and this work would have to be challenged too. One important objection against the phase centre is that it often depends on the direction from the antenna. However, it is often possible to find a phase centre that works over much of the main lobe [11]. It should be taken into account though that the position of this centre may depend on the frequency. These remarks are, of course, also applicable to the magnitude centre. For the purpose of this calibration procedure the magnitude centre only needs to be a valid description along the boresight direction. It is certainly a better approximation than using distances measured from some arbitrary reference plane, which is often chosen for measuring convenience. We will here use ΔR to denote the antenna distance offset, the difference in distance between the reference plane and the magnitude centre. A positive ΔR means a centre position behind the reference plane, see formulas.

If information on the position of the phase or magnitude centre is lacking, it is a fair assumption that ΔR may be on the order of the length of the antenna. Reference [5] even reports the phase centre of these antennas to fall behind the back end of the antennas. A plausible interpretation of this is that the phase velocity in the rear end of the antennas, which is similar to a ridge waveguide, is less than c_0 making the "optical length" of the antenna larger than the physical length. For reflector antennas the situation is more complex. With a flat reflector the phase centre may be expected to be associated with the mirror image of the feeder. I many cases a paraboloidal reflector is used with the purpose of creating a flat wavefront corresponding to a source at infinite distance, although this will not be achieved in the far-field.

At short distances $\Delta R/R$ will often not be negligible but lead to significant and systematic errors in the results. In order to reduce this source of error it is therefore of interest to estimate ΔR so that a correction can be applied to either new or old data and results. However, it is also possible to make the errors largely cancel each other by a proper choice of R_t, R_r and R_d.

Estimating *ΔR* from experimental data

We will here outline one experimental method for estimating the position of the magnitude centre. It is assumed that:

1. Measurements are made under far-field conditions with respect to the antennas.

2. Along the antenna axis in the far-field region the waves propagate as spherical wavefronts originating from a magnitude centre, the position of which may depend on frequency (and polarisation).

3. The medium of propagation is homogenous and transparent, i.e. there is no refraction or absorption.

4. Identical antennas are used.

The antenna distances R_d are measured with respect to some datum plane, e.g. the antenna front, because the position of the magnitude centre is not known.

If measurements are then made between the two antennas at a number of different distances and frequencies and the offset ΔR, i.e. the distance between the reference plane and the magnitude centre would then be:

$$I(R_d, f) = \frac{I_0(f)}{(R_d + 2\Delta R(f))^2}$$

A direct fit of a second-degree curve would give three parameters. In order to avoid the ambiguities that could be associated with calculating I_0 and ΔR from these it is better to rewrite the expression so that only a linear two-parameter fit is needed:

$$\frac{1}{\sqrt{I(R,f)}} = \frac{1}{\sqrt{I_0(f)}}(R + 2\Delta R(f)) = aR + b$$

$$a(f) = \frac{1}{\sqrt{I_0(f)}}$$

$$b(f) = \frac{2\Delta R(f)}{\sqrt{I_0(f)}} \qquad \Leftrightarrow \qquad \Delta R(f) = \frac{b(f)}{2a(f)}$$

It should be remembered that only data points in the far-field region must be used so that the fit involves an extrapolation through the near-field region. This, together with data scatter and the fact that far-field conditions are only reached asymptotically will probably limit the accuracy of the ΔR estimate. It is not unlikely that the phase centre may be determined with better accuracy than the magnitude centre and that the difference in their position, if there is any, is small so that the phase centre inaccuracy combined with the difference is smaller than the position inaccuracy of the magnitude centre making it better to estimate ΔR from the phase centre position. On the other hand, if there is finite difference this could introduce a systematic error.

Cancelling the effects of antenna distance offsets

If the measurement distances R_t and R_r are small compared to the calibration distance R_d systematic errors due to the choice of reference plane for the measurement of antenna distances will not be compensated but affect the results to the fullest extent. This gives an error of $10\lg_{10}\left(\frac{(R_t + \Delta R)^2}{R_t^2}\frac{(R_t + \Delta R)^2}{R_r^2}\right)$ dB, while the error in R_d has little effect since $\frac{\Delta R^2}{R_d^2}$ is small. If $\frac{\Delta R}{R_t} = \frac{\Delta R}{R_r} = 0.1$ and $\frac{\Delta R}{R_d} \approx 0$ the error will be 1.66 dB (and somewhat larger if ΔR is negative).

According to [5] the phase centre of these antennas fall 0.319 m behind the antenna front (but it is not clear if the antenna front plane is at the antenna rim or the protruding ridges). If this applies to the magnitude centre too, this means that the values reported in this work should be raised by

$$\left(\frac{(R_{tr} + \Delta R)^4}{R_{tr}^4}\frac{R_d^2}{(R_d + 2\Delta R)^2}\right) = \left(\frac{(3.28 + 0.319)^4}{3.28^4}\frac{23.07^2}{(23.07 + 2 \cdot 0.319)^2}\right) \approx 1.38 \text{ dB}$$

By using a shorter R_d its relative error will be larger and can be expected to partly cancel the errors in R_t and R_r. In order to find the best conditions for this we will look at the ratio between intensities collected during calibration and measurement. The purpose is find under what conditions this ratio is least affected by ΔR.

$$I_{cal} \propto \frac{1}{(R_d + 2\Delta R)^2} = \frac{1}{R_d^2 + 4R_d\Delta R + 4\Delta R^2}$$

$$I_{meas} \propto \frac{1}{(R_t + \Delta R)^2 (R_r + \Delta R)^2} = \frac{1}{(R_t^2 + 2R_t\Delta R + \Delta R^2)(R_r^2 + 2R_r\Delta R + \Delta R^2)} =$$
$$\frac{1}{R_t^2R_r^2 + 2(R_t^2R_r + R_r^2R_t)\Delta R + 4R_tR_r\Delta R^2 + 2(R_t + R_r)\Delta R^3 + \Delta R^4}$$

Ratio

$$\frac{I_{cal}}{I_{meas}} \propto \frac{R_t^2R_r^2 + 2(R_t^2R_r + R_r^2R_t)\Delta R + 4R_tR_r\Delta R^2 + 2(R_t + R_r)\Delta R^3 + \Delta R^4}{R_d^2 + 4R_d\Delta R + 4\Delta R^2} =$$

$$\frac{R_t^2R_r^2}{R_d^2} \frac{1 + \frac{2(R_t + R_r)\Delta R}{R_tR_r} + \frac{4\Delta R^2}{R_tR_r} + 2\frac{(R_t + R_r)}{R_t^2R_r^2}\Delta R^3 + \frac{\Delta R^4}{R_t^2R_r^2}}{1 + \frac{4\Delta R}{R_d} + \frac{4\Delta R^2}{R_d^2}}$$

If $R_t = R_r = R_d = R$:

$$\frac{I_{cal}}{I_{meas}} \propto \frac{R_t^2R_r^2}{R_d^2} \frac{1 + \frac{4\Delta R}{R} + \frac{4\Delta R^2}{R^2} + \frac{4\Delta R^3}{R^3} + \frac{\Delta R^4}{R^4}}{1 + \frac{4\Delta R}{R} + \frac{4\Delta R^2}{R^2}} = \frac{R_t^2R_r^2}{R_d^2}\left(1 + O(\frac{\Delta R^3}{R^3})\right)$$

Thus, by making this choice of distances the effects of the uncertainties in the antenna reference position can be largely cancelled. If ΔR is as large as 10% of R the contributed error in the result will now be much smaller than previously, $1 + \frac{4\Delta R^3}{R^3} \approx 0.02$ dB.

If the different distances are only approximately equal, $R_t \approx R_r \approx R_d$, a more detailed error analysis should be made. In practice the values of R_t and R_r will vary across the surface and it is therefore preferable to combine ΔR correction and cancellation.

The price for this cancellation is that the use of a short R_d will usually require the use of attenuators which will contribute errors in magnitude and phase.

Note added in proof: Measurements made after the addition of this appendix using methods outlined here indicate ΔR=0.056 m (average over 8.5 to 11.5 GHz). This implies that 0.25 dB should be added to the results of this report. However this was largely cancelled by the use of another reference plan yielding a net error of 0.06 dB to be subtracted.